Unveiling the Intricacies of a Ductile-Phase Toughened Intermetallic: An In-Depth Exploration of a Eutectic Mo–Si–Ti Alloy and its Mechanical Behavior

Raja Jothi Vikram, Shanmukha Kiran Aramanda, Daniel Schliephake, Alexander Kauffmann,* Abhik Choudhury, Martin Heilmaier, and Satyam Suwas

Herein, the development of directional solidification for a novel high-temperature Mo–20Si–52.8Ti (at%) ternary alloy using a modified Bridgeman type apparatus is presented. The resulting alloy exhibits a microstructure consisting of a body-centered cubic solid solution (BCC$_{ss}$) and a hexagonal silicide (Ti,Mo)$_5$Si$_3$ with approximate volume fractions of 50% for each phase. The phases exhibit a crystallographic orientation relationship with $(123)_{BCC_{ss}}||(0001)_{(Ti,Mo)_5Si_3}$ and $[11\bar{1}]_{BCC_{ss}}||[11\bar{2}0]_{(Ti,Mo)_5Si_3}$. Different solidification velocities are imposed, which reveal an inverse relationship to the lamellar spacing according to a Jackson–Hunt type scaling. Mechanical characterization using Vickers indentation demonstrates that the BCC$_{ss}$ accommodates plasticity through dislocation motion, while the silicide phase exhibits high hardness and brittleness, serving as a crack initiation site. Crack propagation is arrested and deflected at the interface to the BCC$_{ss}$. Fracture toughness measurements via indentation yield a fracture toughness of 3.7 MPa$\sqrt{m}$ for the silicide, somewhat higher than previously reported values for Nb-, Mo-, and Cr-based silicides at room temperature. The directionally solidified specimens show an enhanced fracture toughness attributed to a greater BCC$_{ss}$ length scale; thus, combining the ductile and hard phases results in a ductile-phase toughened intermetallic composite. The findings open up new possibilities for the design of advanced intermetallic composites with improved toughness performance.

1. Introduction

As per Carnot's cycle, the efficiency of a system increases with an increase in operating temperatures.[1,2] Hence, there has been a burgeoning commercial demand for materials that can withstand elevated temperatures with enhanced strength and ductility. Existing high-temperature alloys, i.e., superalloys, already operate at very high temperatures near the solvus temperature of their strengthening phases. Aside from technological improvements (such as cooling systems, thermal barrier coating, and microstructural engineering), any further increase in operating temperature is highly improbable.[3–5] This led to a search for alternative metallic structural materials that could endure temperatures higher than around 1100 °C to enhance thermal efficiency. Although intermetallic compounds are potential candidate materials, they are innately brittle and have a low fracture toughness.[6] One of the strategies to enhance the fracture toughness of intermetallic compounds is combining them with a ductile phase, for example, allowing the solidification of the alloy as a eutectic composition. Eutectic systems enable solidification from the liquid leading to lamellar or rod-like microstructure forming an in situ composite balancing strength and ductility.[7] Moreover, eutectics can deliver highly tunable in situ composite microstructures/ properties[8–10] depending on the imposed processing conditions (such as solidification velocity) and material characteristics. Hence, appropriate high-temperature eutectic systems can become potential candidates for replacing the superalloys.

Some recent high-temperature eutectic systems that have been demonstrated to deliver ductile-phase toughened intermetallic composites are Cr–Cr$_3$Si,[11] V–V$_3$Si,[11] Nb–Nb$_3$Si,[11] Cr–Cr$_2$Nb,[12] Nb–Cr$_2$Nb,[13] Ru–RuAl,[14] Cr–Cr$_2$Hf,[13] and Mo–Si based.[4,15] As the latter Mo–Si-based alloys have relatively higher melting temperatures than the other systems, we were inspired to investigate one such alloy system further, as initially developed in refs. [16–19]. Within the Mo–Si–Ti ternary system, a two-phase eutectic Mo–20Si–52.8Ti (in at%) alloy composition comprising body-centered cubic solid solution (BCC$_{ss}$) and

R. J. Vikram, S. K. Aramanda, A. Choudhury, S. Suwas
Department of Materials Engineering
Indian Institute of Science
Bangalore 560012, India

R. J. Vikram, D. Schliephake, A. Kauffmann, M. Heilmaier
Institute for Applied Materials (IAM-WK)
Karlsruhe Institute of Technology (KIT)
76131 Karlsruhe, Germany
E-mail: alexander.kauffmann@kit.edu

The ORCID identification number(s) for the author(s) of this article can be found under https://doi.org/10.1002/adem.202301843.

intermetallic hexagonal silicide phase $(Ti,Mo)_5Si_3$ was found refs. [16–19]. Therein, Ti promotes pesting resistance against the catastrophic oxidation of Mo to MoO_3 and further volatilization at intermediate temperatures between 500 and 800 °C.[16] It also comes along with the added benefit of significantly reduced density.[20–23]

In this study, we focus on a ternary, two-phase eutectic alloy composed of approximately 50% volume fraction of the intermetallic hexagonal silicide phase $(Ti,Mo)_5Si_3$ and BCC_{ss} of (Mo,Ti, Si) where we successfully demonstrate the directional solidification (DS) of the alloy despite its higher liquidus temperature of 1950 °C. Further, the microstructure, texture, and mechanical behavior are explored under two melting conditions, namely, 1) an arc melted; and 2) a DS eutectic (Mo–20Si–52.8Ti) condition. To gain fundamental insights into the solidification behavior of the eutectic alloy, we examine the interplay between processing parameters and microstructures by varying the solidification velocities during DS. The investigations of microstructures encompass morphology selection, length scale selection, orientation relationships (OR), and composition distributions. Furthermore, we assess the mechanical response of each phase through nanoindentation studies. This study provides significant contributions to the field of materials science and engineering, particularly in the area of DS of eutectic alloys. The acquired knowledge and insights can serve as a foundation for the design and development of advanced materials with tailored microstructures and mechanical properties.

2. Experimental Section

2.1. Alloy Design, Vacuum Arc Melting, and DS

Figure 1 represents the liquidus projection of the Mo–Si–Ti phase diagram highlighting the eutectic composition of Mo–20Si–52.8Ti. The expected phases are BCC_{ss} and hexagonal $(Ti,Mo)_5Si_3$. The liquidus temperature of the mentioned eutectic alloy is 1950 °C.
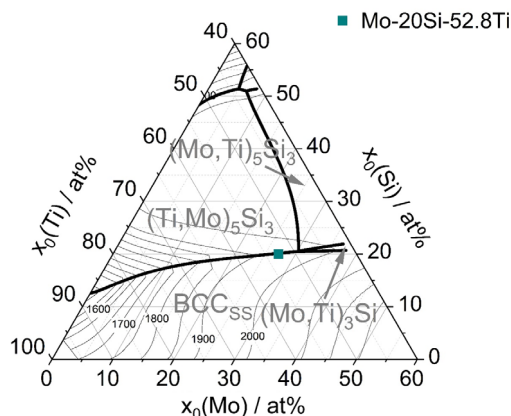

Figure 1. Liquidus projection of the ternary Mo–Si–Ti system with the chemical composition of the currently investigated alloy highlighted as green square. In light gray, the primarily solidifying phases are noted for the different relevant concentration regions.
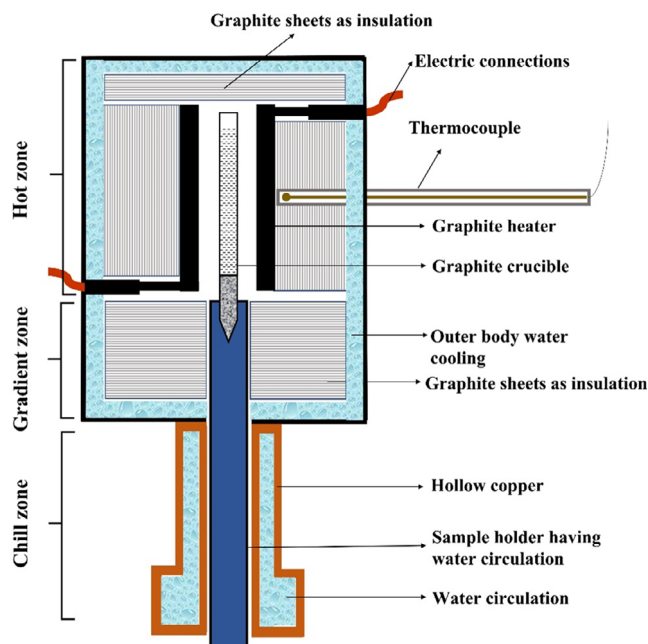

Figure 2. Schematic of the modified Bridgman apparatus developed for high-temperature materials.

Alloys with composition Mo–20Si–52.8Ti (in at%) were prepared by vacuum arc melting (VAM) from the pure elemental constituents and suction casted to form a rod with dimensions of 12 mm diameter and 180 mm height. Subsequently, this rod was electric discharge machined to extract 3 mm diameter specimens of 90 mm height along the longitudinal directions and was placed into cylindrical capillary graphite crucibles of an inner diameter of 3 and 85 mm in height. The samples were directionally solidified utilizing a modified Bridgman-type apparatus, as shown in **Figure 2**. The crucibles containing the samples were positioned in the hot zone at a temperature of 1950 °C, maintained using a graphite heating element. DS experiments were conducted under an argon atmosphere, employing growth rates of 5.0, 10.0, and 20.0 $\mu m\,s^{-1}$ with the assistance of a stepper motor and gearbox. Typically, DS synthesis yielded samples with an overall length of up to 80 mm.

2.2. Characterization Techniques

The samples for microstructural characterization were prepared using conventional metallographic techniques followed by vibratory polishing for 12 h. The microstructure was inspected in a Zeiss Gemini 450 scanning electron microscope (SEM) in backscattered electron (BSE) mode operated at 30 kV and with 13 nA current. Electron backscatter diffraction (EBSD) was used to understand the OR between phases using a high velocity detector camera provided by EDAX manufacturer. The composition of the individual phases was tracked and analyzed using elemental mapping by electron probe microanalys (EPMA, JEOL, JXA-8530F) equipped with both energy and wavelength dispersive spectroscopy detectors. Further, to understand the chemical composition with near-atomic resolution at the interphases,

atom probe tomography (APT) techniques were utilized. The APT data analysis and reconstruction were performed using the IVAS 3.8.4 software package. APT specimens were prepared by standard site-specific in situ-lift-out protocols[24] using a dual-beam SEM/focused ion beam instrument (ThermoFisher Scios) operated at 30 kV. The final cleaning of the APT needles was carried out at 2 kV with a low current of 8 pA to remove the damaged regions caused during prior Ga^+ ion milling.

2.3. Mechanical Testing

The mechanical behavior of the alloys was comprehensively investigated using a combination of microhardness and nanoindentation tests. To assess the toughness of the silicide phase and understand crack bridging and deflection events, a Vickers microhardness testing machine (FUTURE-TECH, FM-810) was employed with a 500 gf load applied for a dwell time of 20 s. To ensure statistical significance, ten indents were made in each phase. Additionally, the toughness of the BCC_{ss} phase was examined using a higher load of 10 kgf, initiating a radial crack from the indented corner. The Qness Q10+ microhardness tester was utilized for these indentations. Subsequently, the crack length was analyzed using a Zeiss LEO EVO 50 SEM operating in secondary electron and BSE modes, with an acceleration voltage of 20 kV.

Nanoindentation experiments were employed to extract the elastic modulus and hardness of the individual phases. A Berkovich nanoindenter (HYSITRON TRIBOINDENTER) was utilized, and the test regions were selected to create a 6×6 matrix, resulting in a total of 36 indentations. This matrix design

ensured a statistically significant confidence level for the load versus displacement curves of each phase. Displacement and load were measured with a resolution of 0.1 nm and 0.1 μN, respectively. The loading rate, unloading rate, and dwell time were consistently maintained for 5 s, with a maximum load approaching 8 mN. By employing the Oliver–Pharr approach, the hardness value H and reduced moduli E_r were determined from the load–displacement curves obtained during the nanoindentation tests[25–27]

$$H = \frac{P_{max}}{A_p} \tag{1}$$

where P_{max} is the maximum load and A_p is the projected contacted area

$$E_r = \frac{\sqrt{\pi}}{2} \frac{dp}{dh} \frac{1}{\sqrt{A_p}} \tag{2}$$

where $\frac{dp}{dh}$, the slope of the unloading curve, is defined as stiffness.

3. Results and Discussions

3.1. Microstructural Characterization

The microstructures of a ternary Mo–Si–Ti alloy under arc-melted conditions were examined using SEM/BSE imaging, and the results are presented in **Figure 3**. The micrographs clearly demonstrate the presence of a bright BCC_{ss} composed of Mo, Ti, and Si, as well as a darker silicide phase
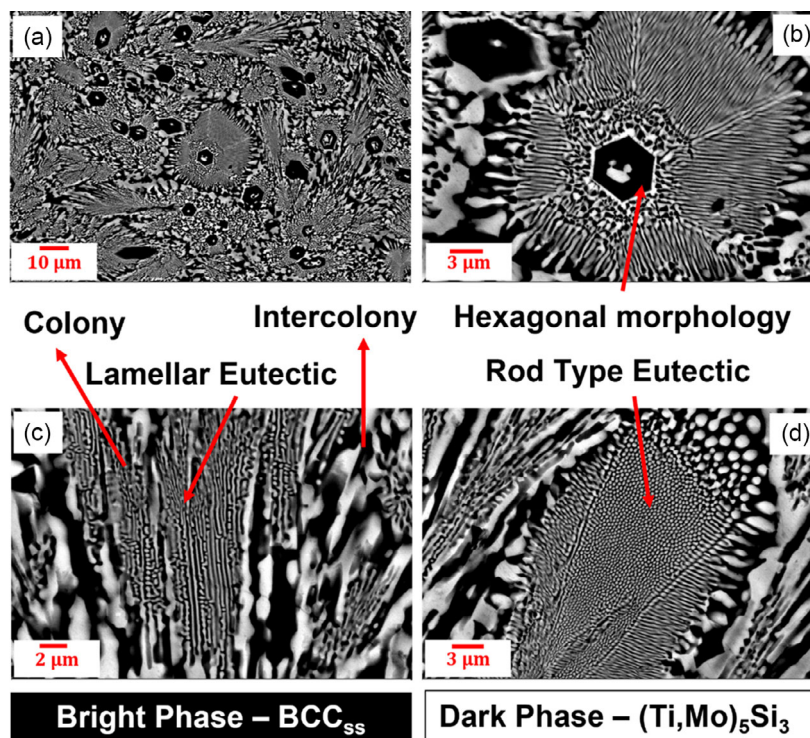

Figure 3. a–d) Transverse section BSE micrograph of the unetched Mo–Si–Ti alloys in VAM specimens to reveal different microstructural features. The bright phase is the $BCC_{ss,}$ and the dark phase is the hexagonal silicide phase.

2301843 (3 of 12)

ADVANCED
SCIENCE NEWS

www.advancedsciencenews.com

ADVANCED
ENGINEERING
MATERIALS

www.aem-journal.com

$(Ti,Mo)_5Si_3$. Notably, the silicide phase exhibits a distorted hexagonal morphology, which can be attributed to its hexagonal crystal structure $D8_8$.[28] Further analysis reveals that the interface of the silicide phase serves as a nucleation site for the growth of lamellae in a coupled manner, as depicted in Figure 3b. Additionally, the micrograph provides evidence of the formation of eutectic colonies, appearing both in lamellar and rod-like forms, as illustrated in Figure 3c,d, respectively. It is worth noting that the spacing between lamellae within the colonies is smaller compared to the spacing observed between different intercolonies.

Figure 4 illustrates the micrograph of DS specimens with varying solidification velocities. To determine the average eutectic spacing, we utilized transverse section images obtained through SEM and employed fast Fourier transform analysis. Multiple images were captured in the vicinity of the sample center, and the eutectic spacing was calculated by averaging the measurements. In Figure 4d, we present a plot of the measured eutectic spacings (λ) corresponding to the eutectic inside the colony against the inverse of the square root of solidification velocity ($V^{-0.5}$). The error bar in the plot represents the standard deviation of the spacing measurements. The obtained data exhibited a linear trend upon fitting. Through this fitting process, we derived the scaling constant for the alloy, which adheres to the Jackson–Hunt type scaling relation.[29]

As observed in Figure 4a–c, the interlamellar spacing increases as the solidification velocity decreases. Also, we witnessed an extinction of eutectic colonies in the DS-5 $\mu m\,s^{-1}$ specimen for the alloy Mo–20Si–52.8Ti. Constitutional supercooling

principles may be responsible for the extinction of colonies below a certain velocity,[30] and the formation of such microstructures below a critical velocity has been reported in refs. [8,31,32] for other ternary alloy systems. The inherent eutectic morphology of the alloy inside the colonies is mixed lamellae and rod-type, as shown in Figure 3a–c, which is a surprising observation considering the volume percent of the phases in the alloy (close to 50%). Rod morphologies are typically found for lower fractions of the minority phase, whereas lamellar/labyrinthine morphologies are typically observed for close to equal volume percentages.[33,34]

We observe a variation in eutectic spacing in the colony and intercolony regions (larger spacing in the intercolony regions than inside the colony) in the samples that exhibit colonies. This could be due to the fact that the intercolony regions are the last solidifying regions. The morphology changes from lamellar to the rod as we move from VAM to the DS specimen, and finally, at a very low solidification rate, a completely degenerated morphology appears, as shown in Figure 4c, for Mo–20Si–52.8Ti.

3.2. Texture Evolution and Orientation Relationship

To gain insights into the texture, phase fraction, and OR between the two phases, EBSD analysis was conducted on the transverse sections of DS specimens. Specifically, the 10 and 5 $\mu m\,s^{-1}$ DS specimens of the Mo–20Si–52.8Ti alloy were analyzed for simplicity. Inverse pole figure (IPF) maps were generated to visualize the orientations of both phases within different colonies, as depicted in **Figure 5**a,e. The IPF maps clearly illustrate that each phase exhibits distinct orientations in different colonies.
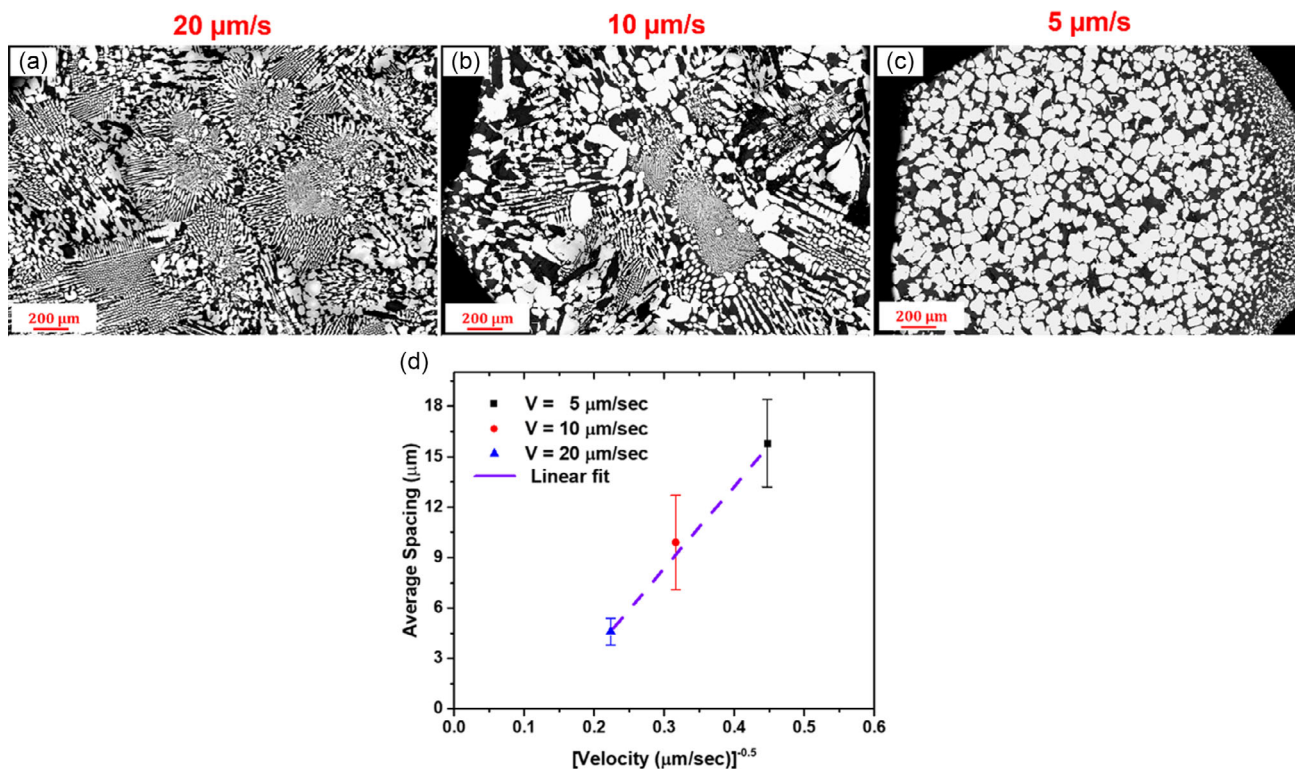

Figure 4. Complete overview of the transverse section micrograph in BSE mode of the DS Mo–20Si–52.8Ti alloy in unetched conditions for the different imposed velocities of a) 20 $\mu m\,s^{-1}$, b) 10 $\mu m\,s^{-1}$, and c) 5 $\mu m\,s^{-1}$. d) Depicts how lamellae spacing varies with solidification velocity.
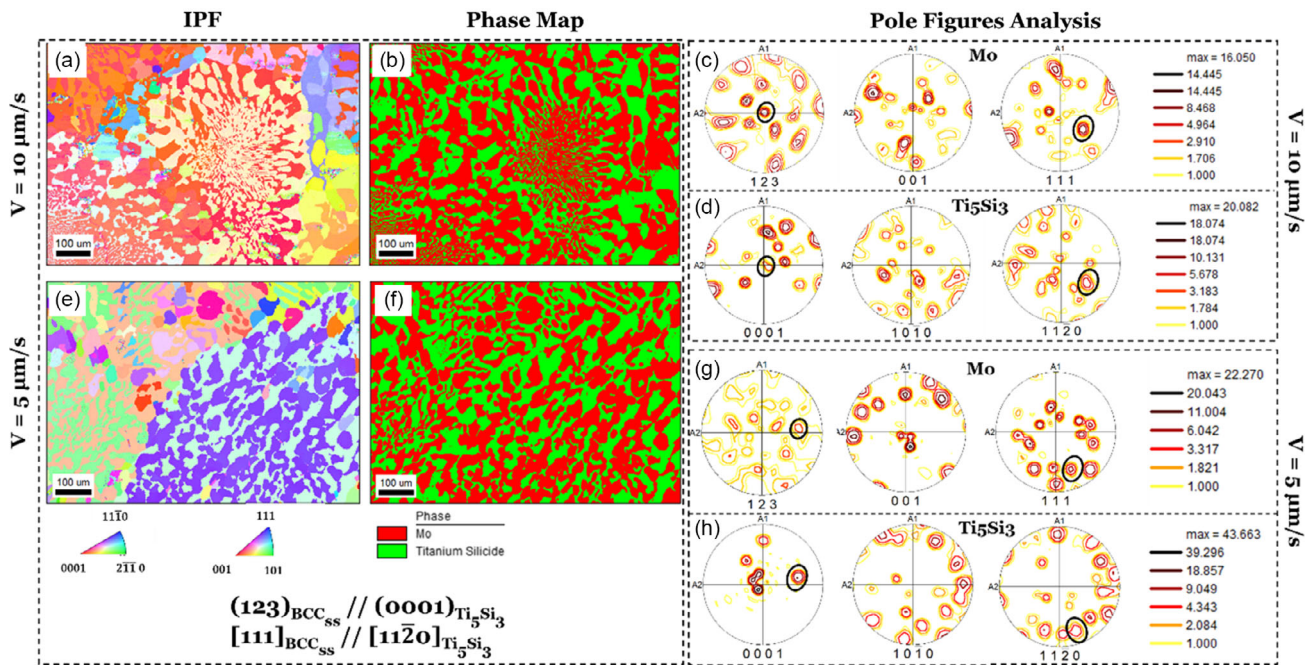
Figure 5. a,e) IPFs, (b,f) phase maps, and c,d,g,h) pole figure analysis to reveal the OR of the two phases in Mo–20Si–52.8Ti solidified at different velocities of 10 and 5 μm s^{-1}, respectively.

Furthermore, the size of the colonies increases as the imposed velocities decrease. The phase map presented in Figure 5b,f demonstrates that the volume fractions of BCC$_{ss}$ and the silicide phases are nearly equal, around 50%. The significant volume fraction and the increase in microstructural length scales of the ductile phase might contribute to enhanced room- and high-temperature fracture toughness, as seen in Section 3.4.

The IPF maps also reveal variations in the initial texture, which can be attributed to differences in cooling rates and solidification velocities. Specimens solidified at higher rates exhibit multiple eutectic colonies with different orientations, leading to an overall weakened texture. Conversely, specimens solidified at slower rates are dominated by a single colony throughout the microstructure, resulting in a stronger texture compared to the faster solidification conditions. Consequently, anisotropic mechanical responses can be anticipated for specimens solidified at different velocities. To determine the OR, EBSD has been utilized on the transverse sections of different specimens (Figure 5).[35,36] Pole figure analysis (Figure 5c,d,g,h) was done to match the pole locations of each phase in the same reference frame to understand the OR. It was identified that the (123) plane of BCC$_{ss}$ is parallel to the basal plane (0001) of (Ti, Mo)$_5$Si$_3$, and the [111] direction of BCC$_{ss}$ is parallel to the [11$\overline{2}$0] of (Ti,Mo)$_5$Si$_3$ with minor deviation, indicating a strong crystallographic OR existing between the phases gives rise to $(123)_{BCC_{ss}}||(0001)_{(Ti,Mo)_5Si_3}$ and $[11\overline{1}]_{BCC_{ss}}||[11\overline{2}0]_{(Ti,Mo)_5Si_3}$. The same OR exists irrespective of changes in solidification velocities.

In general, the most classical OR between hexagonal and BCC phase has been reported to hexagonally closed packed crystal structures (hcp) $(0001)_{hcp}||(110)_{BCC}$ and $[2\overline{1}\,\overline{1}0]_{hcp}||[1\overline{1}1]_{BCC}$,[37] but in the present case the (123) plane maintains parallelism

to the basal plane of the hexagonal system. Rong–Dunlop and Zhang–Kelly have proposed several other hcp/BCC OR where the slip planes do not maintain parallelism.[38–40] The schematics in **Figure 6**a,b represent the atomic arrangement on the parallel planes. The planes of the individual unit cell (BCC$_{ss}$ and hexagonal (Ti,Mo)$_5$Si$_3$) are highlighted in green, while the direction on the plane is highlighted in blue. On the (123) plane of BCC$_{ss}$ phase and (0001) plane of the silicide phase unit cells, a set of atoms on the plane can be connected to form the hexagonal grid. The BCC$_{ss}$ unit cell exhibits a distorted hexagonal lattice that remains parallel to the atoms connected in a hexagonal pattern on the (0001) plane, albeit with a slight misorientation along the c-axis. The deliberate misorientation of the schematic (with different c-axis orientations) allows for better visibility of the atoms on the plane, aiding in understanding the OR more effectively. The OR between the phases plays a crucial role in the growth mechanism and influences the resulting microstructure, which, in turn, affects the mechanical response.[41] The alloy system shows a similar OR irrespective of the cooling and solidification rate, indicating a cooperative coupled growth between the two phases.[41,42]

3.3. Composition Distribution

To investigate the elemental compositional distribution within individual phases, EPMA studies were conducted on the transverse section. EPMA elemental mappings of Mo, Si, and Ti were performed, utilizing different eutectic colonies as reference points in DS specimens with growth velocities of 10 and 20 μm s^{-1}. The elemental mapping results, as depicted in **Figure 7**, provide insights into the average atomic concentrations
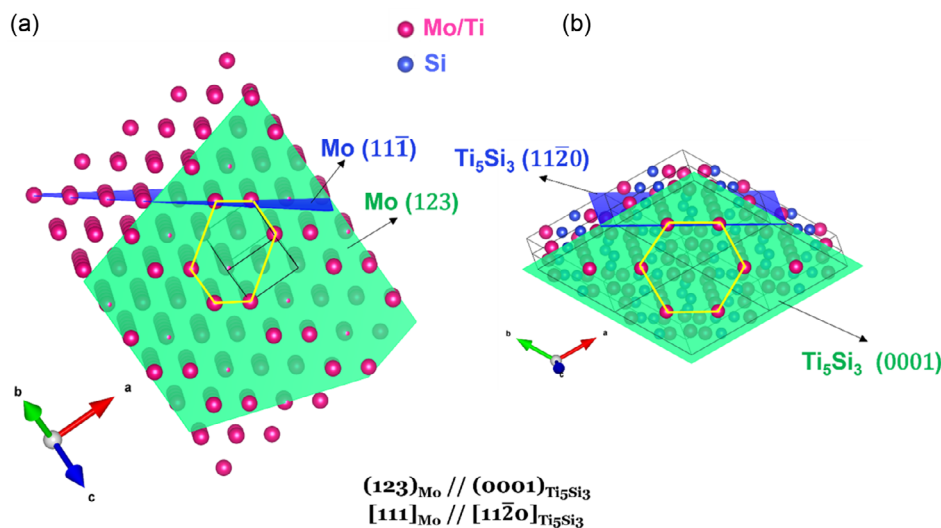
ADVANCED
SCIENCE NEWS

www.advancedsciencenews.com

ADVANCED
ENGINEERING
MATERIALS

www.aem-journal.com

Figure 6. Schematics showing the corresponding planes and directions of the a) BCC_{ss} and b) hexagonal $(Ti,Mo)_5Si_3$ crystals.
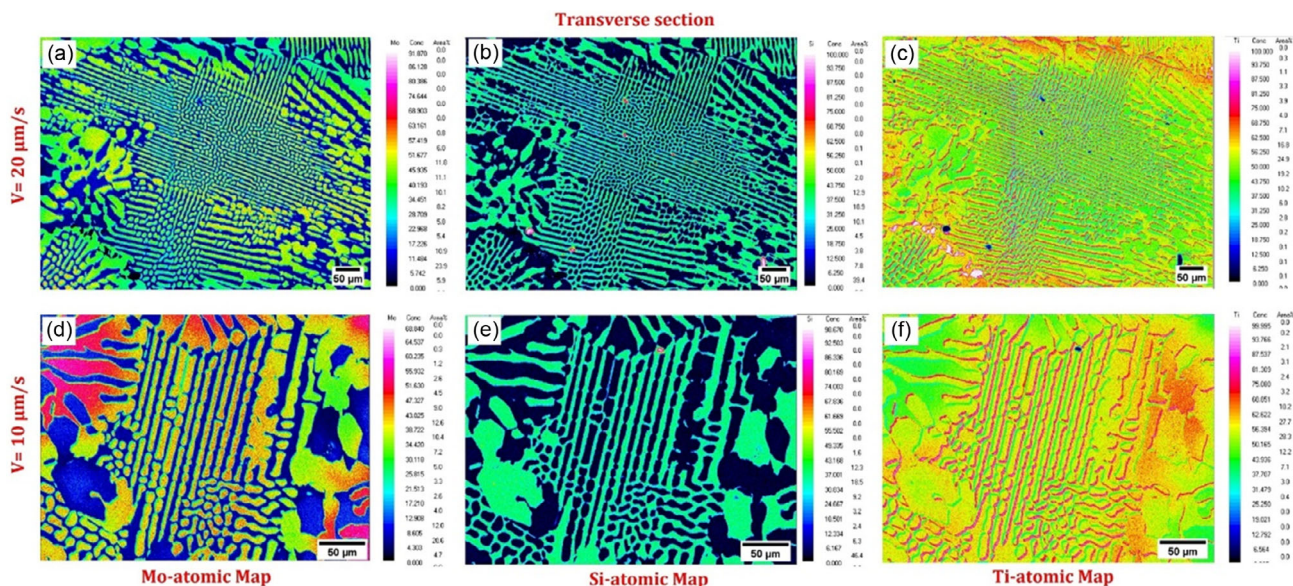

Figure 7. Elemental spectroscopy map of DS Mo–20Si–52.8Ti through EPMA. The mapping was done for individual elements Mo, Si, and Ti in specimens solidified at different velocities a–c) $20\,\mu m\,s^{-1}$ and d–f) $10\,\mu m\,s^{-1}$, respectively.

of Mo, Si, and Ti in the alloy. The overall concentration is determined to be (28 ± 2) at% for Mo, (19 ± 2) at% for Si, and (53 ± 1) at% for Ti. For the silicide phase, the Mo ranges from 12 to 18 at%, Ti ranges from 50 to 56 at%, and the Si ranges from 32 to 38 at%. Consequently, the overall composition turns out to be $(Ti,Mo)_5Si_3$ for the intermetallic hexagonal phase. Notably, the Si concentration in the BCC phase ranges from 1.5 to 2 at%.

The concentration profile observed from the EPMA distribution slightly varied in the colony and intercolony region, but the phase map reveals that only two phases are formed: BCC_{ss} and $(Ti,Mo)_5Si_3$. Ti maps also reveal that Ti is being segregated in the intercolony regions. This could be due to the rejection of Ti from

both the solid phases inside the colony during solidification which already occurs from approximately from 1920 to 1720 °C under equilibrium conditions and extends to even lower temperatures (according to higher Ti contents in the liquid) under nonequilibrium conditions. The coupled growth of the phases is driven by the diffusional gradient existing between the liquids ahead the solid phases being in equilibrium with them. The composition of the liquid in equilibrium with the BCC_{ss} nuclei is rich in Si and Ti, while the liquid in equilibrium with the silicide phase is rich in Mo and Ti. Therefore, there is a concentration gradient that drives this growth. Si and Ti atoms move from the BCC_{ss}–liquid interface to the silicide–liquid interface and vice versa for Mo and Ti atoms. Additionally, the

**ADVANCED
SCIENCE NEWS**

www.advancedsciencenews.com

**ADVANCED
ENGINEERING
MATERIALS**

www.aem-journal.com

composition of individual phases was noted using point scan on the DS specimens (specifically $20 \, \mu m \, s^{-1}$ specimens with larger length scale than arc-melted specimens because of the limitation in the step size of $\approx 2 \, \mu m$), as shown in **Table 1**.

To further understand, the 3D elemental distribution APT technique was employed.[24] **Figure 8**a shows an atom probe reconstruction of a needle-like specimen for the VAM Mo–20Si–52.8Ti with the distribution of Mo (Golden), Si (Blue), and Ti (Green) atoms taken from a phase interface between BCC_{ss} and $(Ti,Mo)_5Si_3$. The left part of the tip correspond to the silicide, while the right corresponds to the BCC_{ss}. The composition profiles across interfaces, as shown in Figure 8b, reveal a high amount of Ti (≈ 52 at%) and Si (≈ 37 at%) with a much lower content of Mo (≈ 9 at%) in the silicide phase while a high amount of Mo (≈ 62 at%) and Ti (≈ 36 at%) and lower amount of Si (≈ 2 at%) at the interface of BCC_{ss} phase. The composition of the silicide phase appears uniform without any observed gradient at the

Table 1. Composition of BCC_{ss} and $(Ti,Mo)_5Si_3$ phases.

Phase	Mo [at%]	Ti [at%]	Si [at%]
$(Ti,Mo)_5Si_3$	9.4	53.3	37.3
BCC_{ss}	43.9	54.2	1.9

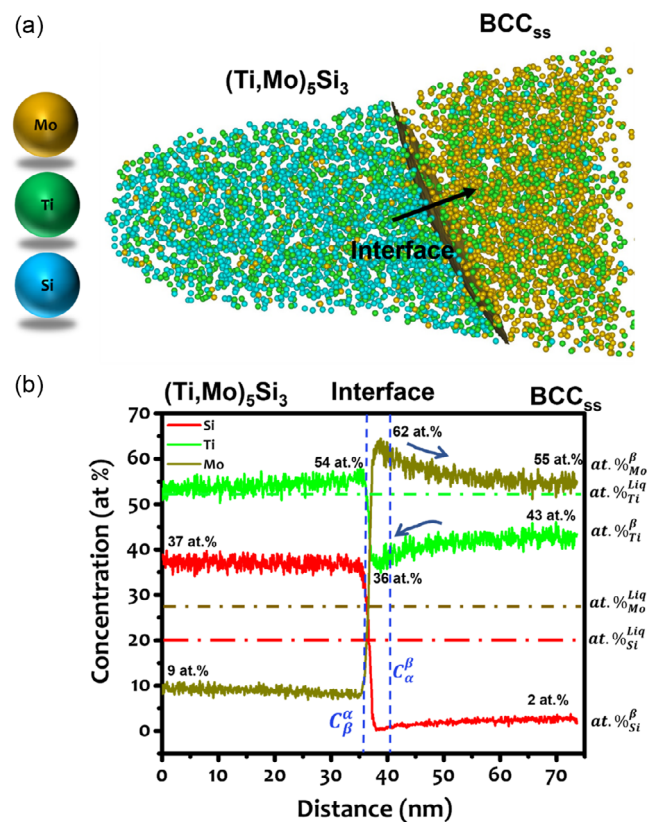**Figure 8.** a) An APT reconstruction with the distribution of Mo, Ti, and Si atoms across a $BCC_{ss}/(Ti,Mo)_5Si_3$ interphase for the VAM Mo–20Si–52.8Ti. b) Composition profiles taken across the interphase into the bulk of both phases. For simplicity the α phase is referred to as BCC_{ss} and the β phase is referred to as $(Ti,Mo)_5Si_3$.

interface. This observation is strongly correlated with the intermetallic nature of the phase, which exhibits a fixed stoichiometry. Conversely, the BCC_{ss} phase displays a gradient at the interface. Specifically, there is a downhill gradient for Mo and an uphill gradient for Ti toward the bulk of the BCC_{ss} phase. In contrast, the Si concentration remains relatively constant. This suggests that the maximum solid solubility of Si in the BCC_{ss} phase is 2 at%, which agrees well with the data reported in Table 1. The observed interface segregation is related to the composition distribution within the solid phases and the liquid phase during growth and their diffusion along the nonplanar solidification front as well as the diffusion during further cooling to room temperature. Ti seems enriched at the tip of the growing BCC_{ss} while Mo is enriched in the grooved region between the two solid phases.

3.4. Mechanical Behavior

3.4.1. Microindentation Approach

Vickers microindentation was employed to investigate the behavior of individual phases under a specific load. **Figure 9**a,c depicts the indent mapping on BCC_{ss} and $(Ti,Mo)_5Si_3$ in DS Mo–20Si–52.8Ti ($20 \, \mu m \, s^{-1}$) specimens. The indentation on the BCC_{ss} reveals the presence of shear bands, indicating its ability to accommodate plastic deformation as revealed in Figure 9b. On the other hand, the indentation on the silicide phase exhibits crack initiation and propagation from the indent corners, where the stress concentration is maximum, as shown in Figure 9b. This suggests the intrinsic brittleness of the silicide phase at room temperature. However, it is noteworthy that the cracks initiated in the brittle silicide phase are arrested and deflected once they encounter the ductile BCC_{ss} phase. This interaction between the phases retards the propagation of cracks, as shown in Figure 9c,d.

It is known that the toughness of a material increases if there is a retardation either in the crack initiation or crack propagation stage, and if such a phenomena happens with a combination of ductile and brittle phases like a composite of brick and mortar.[6] BCC_{ss} is in the present case more ductile than the hexagonal silicide phase. A crack-bridging event can occur with a continuous alternate ductile phase in the eutectic colonies, leading to additional toughening. Ashby pointed out that presence of a ductile phase in a brittle material increases fracture toughness and is a strong function of its volume fraction, elastic modulus, yield strength, and length scale of the ductile phase.[43,44] Two major events, such as crack bridging and deflection, increase fracture toughness, which strongly depend on the distribution of the ductile phase.[43,45] The intercolony regions observed in Figure 3 showed larger phase spacing than intracolony regions. Thus, a significant contribution to the fracture toughness stems from the intercolony region due to the considerable absorption of plastic energy related to the extension of the ductile phase. Additionally, the eutectic colony center also contributes to fracture toughness due to a series of crack bridging events as a function of the thickness of ductile phase. However, colony size or lamellar spacing should not be reduced to such an extent that the critical crack length is equal or greater than lamellar spacing; if that happens, the crack propagates in uncontrolled way in the lamellar eutectic structure. The phase map from Figure 5 showed

**ADVANCED
SCIENCE NEWS**

www.advancedsciencenews.com

**ADVANCED
ENGINEERING
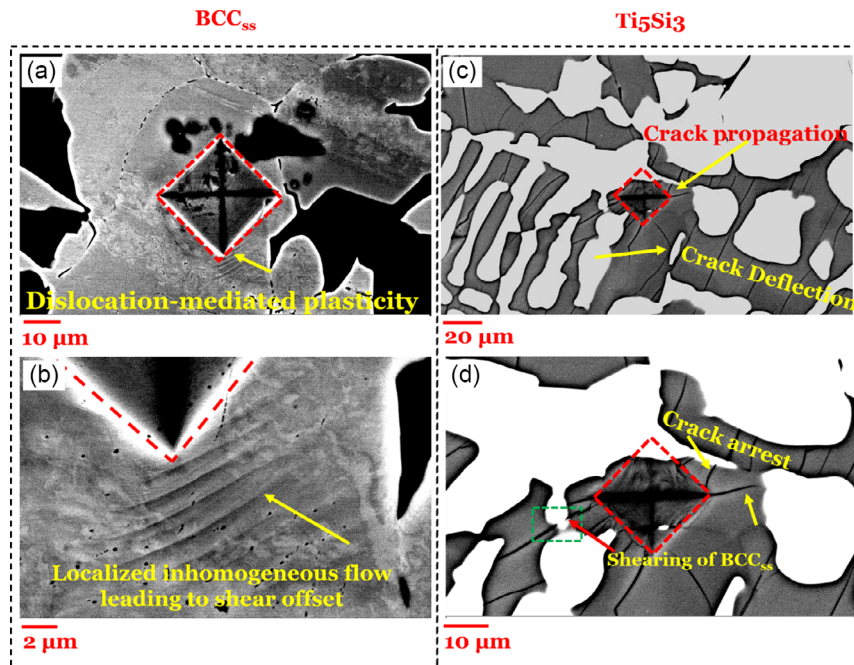MATERIALS**

www.aem-journal.com

Figure 9. a) The indent mapping on BCC$_{ss}$ and b) its corresponding high magnification micrograph showing plastic flow response; c) the indent on (Ti,Mo)$_5$Si$_3$ and d) its corresponding high magnification micrograph showing cracking events emanating from the indent corners.

that the volume fraction of each phase does not change irrespective of the imposed withdrawal velocity. For the same volume fraction of two phases BCC$_{ss}$ and (Ti,Mo)$_5$Si$_3$, an increase in the length scale of the ductile phase, for example, by lower withdrawal rate during DS, translates into a higher probability for the moving crack to interact with the ductile matrix to undergo shear deformation and to get trapped. If the length scale is small and the lamellae are continuous, a crack-bridging event may happen for the moving cracks; if it is discontinuous like a broken lamellar structure, the moving crack does not move through the ductile phase and propagate quickly adjacent to brittle regions.[35,44] The fine-scaled microstructure is good at achieving high strength at low temperatures. However, the increase in the length scale plays a crucial role in enhancing the fracture toughness, which can be achieved by a change in solidification rate. It can be seen from Figure 9d that a crack can shear the ductile phase, leading to cracking if its length scale is small. A significant amount of plastic energy is dissipated in the ductile phase, enhancing the overall toughness of the material. This interfacial cracking also has the potential to get delaminated at the interface, which was not evidenced in the present study. The combination of crack arrest, crack renucleation, and crack deflection enhances fracture toughness. Therefore, based on the above concept, the fracture toughness of specimens solidified with slow velocities exhibits higher enhancement in fracture toughness due to larger length scales.

3.4.2. Nanoindentation Approach

To assess the mechanical behavior of individual phases accurately, such as hardness and elastic modulus, nanoindentation using the Oliver and Pharr approach was utilized.[46] **Figure 10**d represents the typical load–displacement curves of BCC$_{ss}$, the interface, and the (Ti,Mo)$_5$Si$_3$ phase, respectively. A region and spacing were selected in such a manner that a 6×6 indent mapping is created and gives equal statistical accuracy in measuring the properties of the individual phase, as shown in Figure 10a–c. The important parameters from the load versus displacement curve are listed in **Table 2**.

As shown in Figure 10d, pop-in events are evidenced in the load versus displacement curve of the (Ti,Mo)$_5$Si$_3$ silicide phase. The pop-ins are plainly visible, but the displacement burst magnitude is low due to the intermetallic phase's intrinsic brittleness, which precludes less or no plastic strain accumulation at room temperature. These pop-in events are generally caused by dislocation activity, twinning, slip, and sometimes even cracking and are referred to as localized incipient plasticity (sudden elastic to plastic transition) under indentation load.[47–49] A displacement burst in the silicide phase indicates that dislocations nucleate initially, but the resistance to its motion is increased due to the ordered nature of intermetallics which is associated with certain faults, and at a higher load a crack can be induced. As evidenced, cracking was prominent with the (Ti,Mo)$_5$Si$_3$ phase due to intrinsic brittle characteristics, which means the pop-in is substantiated with cracking events when resolved stress crosses a threshold limit. Also, there were no pop-in events for the loading curve of the BCC$_{ss}$ phase. The load versus displacement curve of (Ti,Mo)$_5$Si$_3$, the interface, and the BCC$_{ss}$ phase reveal the shift in indent depth while moving from a hard to a soft region. The reduced elastic modulus and hardness are higher for the silicide phase than the ductile BCC$_{ss}$ phase. The onset of plasticity for the silicide phase can be obtained by fitting the Hertz contact model extrapolated to the measured load versus
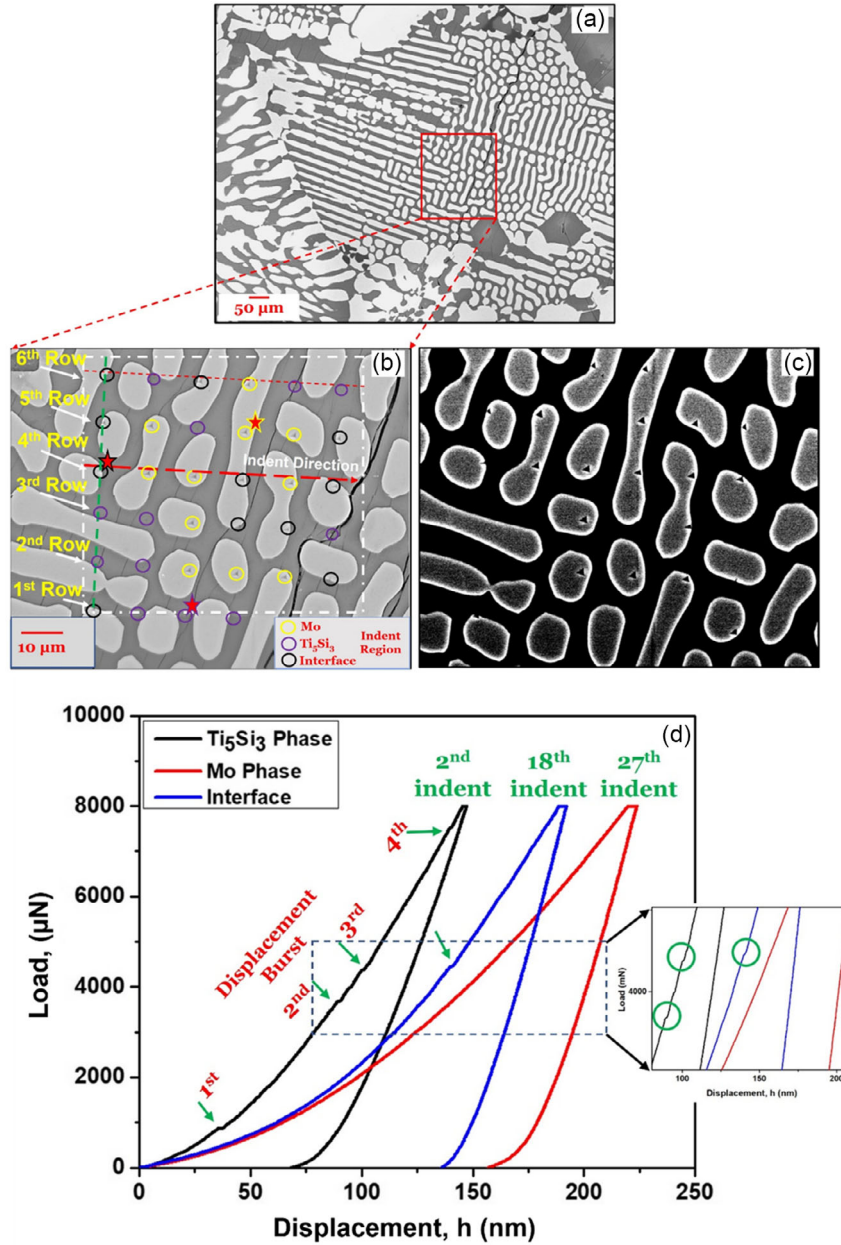
Figure 10. BSE micrograph showing a) the region of interest for nanoindentation tests, b) regions with 6 × 6 matrix indicating nanoindents from row 1 to row 6, c) A–B topo mode for making the indents visible on the BCC_{ss} phase, and d) the load versus displacement curve for the BCC_{ss} (red), the interface (blue), and $(Ti,Mo)_5Si_3$ (black) phases for the Mo–20Si–52.8Ti.

Table 2. The reduced elastic modulus and hardness of $(Ti,Mo)_5Si_3$ and BCC_{ss} phase obtained from oliver and Pharr approach.

Parameters	BCC_{ss}	$(Ti,Mo)_5Si_3$
E_r [GPa]	157 ± 4	204 ± 10
H [GPa]	6 ± 0.1	16 ± 0.8

$$P = \frac{4}{3} \, E_r \, R^{\frac{1}{2}} \, h^{\frac{3}{2}} \tag{3}$$

where R is the indenter tip radius of curvature, and E_r is the reduced modulus. Considering the deformation before the pop-in event is purely elastic, the maximum shear stress (at elastic to plastic transition) beneath the indenter tip, τ_{max}, is expressed as follows

displacement curve. The critical load at the onset of pop-in is given by refs. [25,48].

$$\tau_{max} = 0.18 \left(\frac{E_r}{R} \right)^{\frac{2}{3}} P^{\frac{1}{3}} \tag{4}$$

**ADVANCED
SCIENCE NEWS**

www.advancedsciencenews.com

**ADVANCED
ENGINEERING
MATERIALS**

www.aem-journal.com

where $P = 975\,\mu N$ (the first pop-in) as shown in Figure 10d and upon substituting in Equation (4), we get the maximum shear stress calculated as 5.3 GPa, which is approximately 1/14th of the 78 GPa shear modulus calculated from elastic modulus with an assumed Poisson's ratio of 0.3.

To understand the fracture toughness of the silicide phase, the indentation method is employed via radial crack theory. Hyun et al.[50,51] examined the effects of material properties on the crack size formed by Vickers indentation and suggested a regression formula for the estimation of the fracture toughness

$$K_Q = \alpha \left(\sqrt{\frac{E_r}{H}} \right) \left(\frac{P_{max}}{c^{\frac{3}{2}}} \right) \tag{5}$$

where P_{max} is the maximum indentation load (500 gf), c is the radial crack length achieved for a particular load (18 μm), and α is an empirical constant that depends on the geometry of the indenter tip (here $\alpha = 0.016$[52]). Based on the results, the fracture toughness obtained was 3.7 MPa$\sqrt{m}$. The fracture toughness value obtained is highest among the reported Nb-, Mo-, and Cr-based silicides at room temperature,[35] and combining with the BCC$_{ss}$ phase results in a ductile-phase toughened intermetallic as discussed in Section 3.4.1.

Based on the properties of the individual phases and combined strength achieved, the overall fracture toughness can be quantitively estimated through empirical relationships. As per the proposed fracture toughness theory from previous studies, the increase in fracture toughness is proportional to the product of the strength σ_o of the combined or individual phases, the volume fraction V_{Duc}, and the size of the ductile phase $L_{Duc.}$[53,54] The empirical relation is given below

$$\Delta K_Q = \sqrt{E\, C\, \sigma_o\, V_{Duc}\, L_{Duc}} \tag{6}$$

where ΔK_Q is the increase in fracture toughness due to the presence of a ductile phase in the microstructure, and E is the elastic modulus. The parameter C is a material constant representing the degree of constraint imposed upon a ductile particle from the matrix and is ≈ 1.6[44,55] when the ductile particle plastically deforms and fails without interface decohesion. The degree of constraint might vary from 1 to 6. The Ashby model[54] assigns C values based on failure mechanisms such as internal void growth, decohesion at the metal–matrix interface, and cracking in the brittle matrix. The constraint value is usually 1.6 when the ductile phase plastically deforms and fails without interface decohesion, as seen in our indentation hardness micrographs (Figure 9).

Table 3 shows the overall fracture toughness for the VAM and DS counterpart where $V_{BCC_{ss}}$, $L_{BCC_{ss}-BCC_{ss}}$, $L_{BCC_{ss}-(Ti, Mo)_5 Si_3}$, and σ_o denote the volume fraction and length scale of BCC$_{ss}$ phase, interlamellar spacing, and yield strength estimation of ductile phase taken from hardness values typically 2.4 HV.[27] Assuming the microstructure is stable till 1000 °C for these high-temperature alloys, the fracture toughness (ΔK_Q) enhancement is much higher for DS specimens as compared to the VAM microstructure. The maximum enhancement is for the specimens solidified with the lowest imposed velocity in the case of Mo–20Si–52.8Ti because of the largest increase in

Table 3. Strength and microstructural parameters of different specimens for evaluating the enhancement in fracture toughness.

Parameters	Mo–20Si–52.8Ti			
	VAM	DS		
		20 μm s^{-1}	10 μm s^{-1}	5 μm s^{-1}
$V_{BCC_{ss}}$	0.55	0.53	0.56	0.55
$V_{(Ti,Mo)_5 Si_3}$	0.45	0.47	0.44	0.45
$L_{BCC_{ss}-BCC_{ss}}$ [μm]	0.19	2.2	4.6	8.6
$L_{BCC_{ss}-(Ti,Mo)_5 Si_3}$ [μm]	0.34	4.3	10.1	17.1
σ_o [MPa]	1320	590	420	230
ΔK_Q [MPa$\sqrt{m}$]	6	13	16	16

microstructural length scales. The ΔK_Q is lowest for VAM specimens because of the very fine scale microstructure.

Overall, the cracks initiated in the brittle phase propagate drastically once they reach the critical crack length a_c. The crack propagation is arrested at the interface of the ductile phase. Thus, a series of crack arrest/deflection events at the interface will enhance fracture toughness. Looking into the microstructural parameters for the eutectic Mo–20Si–52.8Ti alloy, the volume fraction remained constant throughout different DS specimens, which means the increase in the ductile phase's length scale leads to an increase in the length scale of the brittle phase. The finer microstructure enhances strength, but due to the ductile phase's fine length scale, a very small fraction of the energy is absorbed while the remaining is passed to the neighboring brittle phase; thus, fracture toughness increases to a smaller extent in arc-melted specimen even though they exhibit high strength which plays a huge role in ΔK_Q (refer to Equation (6)). If the length scale is optimized such that moving cracks are retarded through both bridging and deflection events, an enhanced fracture toughness can be achieved in the DS specimens. Thus, based on the above discussion, a microstructure consisting of fine colonies and coarse intercolonies would be advantageous in terms of enhancing both toughness and strength.

3.4.3. Indentation Fracture Toughness

To assess the effective indentation fracture toughness of the Mo–20Si–52.8Ti alloy, the Vickers macroindentation method was employed using a very large load of HV 10 (10 kgf), as shown in **Figure 11**. This method aimed to generate cracks in the BCC$_{ss}$ phase and the silicide phase radially from the corner of the indenter tip. The regions of interest for this study were lamellar structures consisting of an equal fraction of the individual phases. The elastic modulus for the two-phase microstructure and the elastic modulus values obtained from nanoindentation technique were averaged out. Under the load of 98 N, the observed radial crack length at room temperature was approximately 59 μm. By using Equation (6), the indentation fracture toughness of the Mo–20Si–52.8Ti alloy was obtained to be 18 MPa$\sqrt{m}$, as explained in Section 3.4.2.

The reported fracture toughness value is relatively higher compared to Nb-, Mo-, and Cr-based silicides at room temperature.
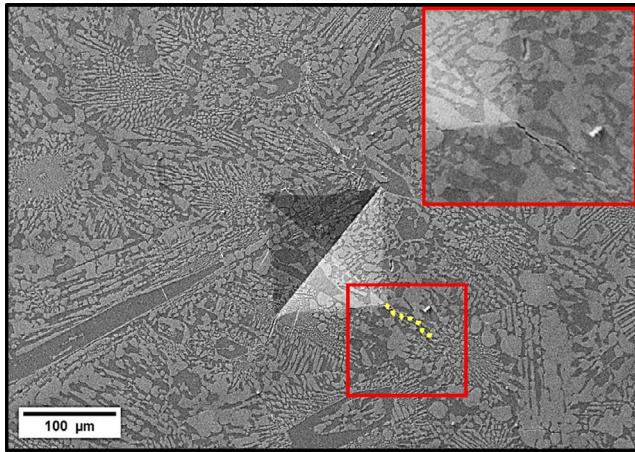
Figure 11. SEM micrograph of the Vickers indentation and cracks at test loads of 10 kgf for the VAM Mo–20Si–52.8Ti alloy.

Table 4. Indentation fracture toughness obtained for eutectic alloy and the silicide phase.

	E [GPa]	H [GPa]	P_{max} [N]	c [μm]	α	ΔK_Q [MPa$\sqrt{m}$]
Mo–20.0Si–52.8Ti	180	6.6	98	58	0.016	18
$(Ti,Mo)_5Si_3$	204	16.6	4.9	18	0.016	3.7

This can be attributed to the high fraction of Ti in the BCC_{ss} phase in the microstructure of the alloy. **Table 4** also provides the fracture toughness value for the silicide phase. The utilization of the Vickers macroindentation method, along with the analysis of lamellar structures, allowed for the evaluation of effective fracture toughness of Mo–20Si–52.8Ti. The measured fracture toughness highlights the superior toughness of the alloy, mainly due to the composition and microstructural distribution of the BCC_{ss} phase.

4. Conclusions

In this article, we explored the role of cooling and solidification rate on the microstructure formation of a eutectic Mo–Si–Ti alloy containing BCC_{ss} and hexagonal $(Ti,Mo)_5Si_3$ silicide phase. Different solidification velocities were imposed, and it was found that the lamellae/rod spacing tends to increase with a decrease in velocities and obeys a Jackson–Hunt type scaling law. The OR between BCC_{ss} and silicide phase is identified to $(123)_{BCC_{ss}}||(0001)_{(Ti,Mo)_5Si_3}$ and $[11\bar{1}]_{BCC_{ss}}||[11\bar{2}0]_{(Ti,Mo)_5Si_3}$. EPMA reveals the segregation of Ti in the intercolony regions.

At room temperature, the BCC_{ss} is ductile and accommodates plasticity through dislocation motion. The silicide phase was found to be harder and brittle and acts as a crack initiation site. It was observed that crack propagation was retarded at the BCC_{ss} interface, resulting in a ductile-phase toughened intermetallic. The eutectic alloy showed enhanced strength in VAM condition and enhanced fracture toughness response in the DS condition. The indentation fracture toughness values obtained for the

silicide phase is the highest among the reported Nb-, Mo-, and Cr-based silicides at room temperature.

Conflict of Interest

The authors declare no conflict of interest.

Data Availability Statement

The data that support the findings of this study are available from the corresponding author upon reasonable request.

[1] N. L. S. Carnot, S. W. Thomson, *Reflections on the Motive Power of Heat, Accompanied by An Account of Carnot's Theory*, John Wiley & Sons, New York, Chapman & Hall, Limited, London **1897**.

[2] A. Saini, T. Pollock, *MRS Bull.* **2012**, *37*, 550.

[3] B. P. Bewlay, M. R. Jackson, P. R. Subramanian, *JOM* **1999**, *51*, 32.

[4] D. M. Dimiduk, J. H. Perepezko, *MRS Bull.* **2003**, *28*, 639.

[5] A. K. Bhambri, T. Z. Kattamis, J. E. Morral, *Metall. Trans. B* **1975**, *6*, 523.

[6] H. Bei, G. M. Pharr, E. P. George, *J. Mater. Sci.* **2004**, *39*, 3975.

[7] S. Akamatsu, M. Plapp, *Curr. Opin. Solid State Mater. Sci.* **2016**, *20*, 46.

[8] S. Mukherjee, S. K. Aramanda, S. S. Legese, A. Riss, G. Rogl, O. E. Femi, E. Bauer, P. F. Rogl, K. Chattopadhyay, *ACS Appl. Energy Mater.* **2021**, *4*, 11867.

[9] A. A. Kulkarni, J. Kohanek, K. I. Tyler, E. Hanson, D.-U. Kim, K. Thornton, P. V. Braun, *Adv. Opt. Mater.* **2018**, *6*, 1800071.

[10] J. H. Han, K. B. Kim, S. Yi, J. M. Park, S. W. Sohn, T. E. Kim, D. H. Kim, J. Das, J. Eckert, *Appl. Phys. Lett.* **2008**, *93*, 141901.

[11] B. P. Bewlay, J. A. Sutliff, M. R. Jackson, K. M. Chang, *Mater. Manuf. Processes* **1994**, *9*, 89.

[12] K. Li, S. Li, Y. Xue, H. Fu, *Int. J. Refract. Met. Hard Mater.* **2013**, *36*, 154.

[13] D. M. Shah, D. L. Anton, D. P. Pope, S. Chin, *Mater. Sci. Eng., A* **1995**, *192–193*, 658.

[14] N. Llić, R. Rein, M. Göken, M. Kempf, F. Soldera, F. Mücklich, *Mater. Sci. Eng., A* **2002**, *329–331*, 38.

[15] J. H. Schneibel, in *Proc. of the 17th Annual Conf. on Fossile Energy Materials*, Baltimore, MD, April **2003**, pp. 3–9.

[16] D. Schliephake, A. Kauffmann, X. Cong, C. Gombola, M. Azim, B. Gorr, H. J. Christ, M. Heilmaier, *Intermetallics* **2019**, *104*, 133.

[17] S. Burk, B. Gorr, H. J. Christ, D. Schliephake, M. Heilmaier, C. Hochmuth, U. Glatzel, *Scr. Mater.* **2012**, *66*, 223.

[18] Y. Yang, Y. A. Chang, L. Tan, Y. Du, *Mater. Sci. Eng., A* **2003**, *361*, 281.

[19] R. Mitra, V. V. Rama Rao, *Mater. Sci.* **1998**, *29*, 1665.

[20] S. Majumdar, B. Paul, P. K. Singh, J. Kishor, V. Kain, *Intermetallics* **2018**, *100*, 126.

[21] M. A. Azim, B. Gorr, H. J. Christ, O. Lenchuk, K. Albe, D. Schliephake, M. Heilmaier, *Intermetallics* **2017**, *90*, 103.

[22] Q. Lu, Y. Hao, Y. Wang, P. Feng, J. Fan, *Corros. Sci.* **2019**, *161*, 108180.

[23] S. Obert, A. Kauffmann, R. Pretzler, D. Schliephake, F. Hinrichs, M. Heilmaier, *Metals* **2021**, *11*, 169.

[24] S. K. Makineni, M. Lenz, P. Kontis, Z. Li, A. Kumar, P. J. Felfer, S. Neumeier, M. Herbig, E. Spiecker, D. Raabe, B. Gault, *JOM* **2018**, *70*, 1736.

[25] C. A. Schuh, *Mater. Today* **2006**, *9*, 32.

[26] Y. Mazaheri, A. Kermanpur, A. Najafizadeh, *Mater. Sci. Eng., A* **2015**, *639*, 8.

[27] M. D. Taylor, K. S. Choi, X. Sun, D. K. Matlock, C. E. Packard, L. Xu, F. Barlat, *Mater. Sci. Eng., A* **2014**, *597*, 431.

[28] K. Kishida, T. Fukuyama, T. Maruyama, H. Inui, *Sci. Rep.* **2020**, *10*, 17983.

[29] K. A. Jackson, J. D. Hunt, in *Dynamics of Curved Fronts* (Ed: P. Pelcé), Academic Press, San Diego **1988**, pp. 363–376, https://doi.org/10.1016/B978-0-08-092523-3.50040-X.

[30] W. W. Mullins, R. F. Sekerka, *J. Appl. Phys.* **1964**, *35*, 444.

[31] S. K. Aramanda, S. K. Salapaka, S. Khanna, K. Chattopadhyay, A. Choudhury, *Acta Mater.* **2020**, *197*, 108.

[32] S. K. Aramanda, K. Chattopadhyay, A. Choudhury, *Acta Mater.* **2021**, *221*, 117400.

[33] S. Liu, J. H. Lee, R. Trivedi, *Acta Mater.* **2011**, *59*, 3102.

[34] A. Parisi, M. Plapp, *EPL* **2010**, *90*, 26010.

[35] R. Mitra, *Int. Mater. Rev.* **2006**, *51*, 13.

[36] H. Bei, E. P. George, *Acta Mater.* **2005**, *53*, 69.

[37] Y. Matsukawa, I. Okuma, H. Muta, Y. Shinohara, R. Suzue, H. L. Yang, T. Maruyama, T. Toyama, J. J. Shen, Y. F. Li, Y. Satoh, S. Yamanaka, H. Abe, *Acta Mater.* **2017**, *126*, 86.

[38] Y. Liu, D. Zhao, X. Nie, H. Tao, J. Wang, J. Gui, *Philos. Mag. Lett.* **2012**, *92*, 668.

[39] M. X. Zhang, P. M. Kelly, *Prog. Mater. Sci.* **2009**, *54*, 1101.

[40] M. X. Zhang, P. M. Kelly, *Acta Mater.* **2005**, *53*, 1073.

[41] F. Zhang, H. Feng Wang, C. Lai, J. Bao Zhang, Y. Chan Zhang, Q. Zhou, *Trans. Nonferrous Met. Soc. China* **2020**, *30*, 1826.

[42] E. G. Castle, A. M. Mullis, R. F. Cochrane, *Acta Mater.* **2014**, *77*, 76.

[43] N. Sekido, Y. Kimura, S. Miura, F. G. Wei, Y. Mishima, *J. Alloys Compd.* **2006**, *425*, 223.

[44] J. A. Lemberg, R. O. Ritchie, *Adv. Mater.* **2012**, *24*, 3445.

[45] Z. Li, L. M. Peng, *Acta Mater.* **2007**, *55*, 6573.

[46] W. C. Oliver, G. M. Pharr, *J. Mater. Res.* **1992**, *7*, 1564.

[47] B. Bor, D. Giuntini, B. Domènech, M. V. Swain, G. A. Schneider, *J. Eur. Ceram. Soc.* **2019**, *39*, 3247.

[48] F. Pöhl, *Sci. Rep.* **2019**, *9*, 15350.

[49] S. Vadalakonda, R. Banerjee, A. Puthcode, R. Mirshams, *Mater. Sci. Eng., A* **2006**, *426*, 208.

[50] H. C. Hyun, F. Rickhey, J. H. Lee, M. Kim, H. Lee, *Eng. Fract. Mech.* **2015**, *134*, 304.

[51] C. Li, F. Zhang, X. Wang, X. Rao, *Appl. Opt.* **2018**, *57*, 3661.

[52] D. Ćorić, L. Ćurković, M. M. Renjo, *Trans. FAMENA* **2017**, *41*, 1.

[53] M. F. Ashby, F. J. Blunt, M. Bannister, *Acta Metall.* **1989**, *37*, 1847.

[54] K. Kishida, T. Maruyama, T. Fukuyama, H. Inui, *Sci. Technol. Adv. Mater.* **2020**, *21*, 805.

[55] D. R. Bloyer, K. T. Venkateswara Rao, R. O. Ritchie, *Mater. Sci.* **1998**, *29*, 2483.

2301843 (12 of 12)